



Published in final edited form as:

Nature. 2020 March ; 579(7798): 256–259. doi:10.1038/s41586-020-2062-x.

Recurrent interactions in local cortical circuits

Simon Peron^{1,2,*}, Ravi Pancholi², Bettina Voelcker², Jason D. Wittenbach¹, H. Freyja Ólafsdóttir^{1,3,4,*}, Jeremy Freeman¹, Karel Svoboda¹

¹:Janelia Research Campus (HHMI)

²:Center for Neural Science, New York University

³:Department of Cell and Developmental Biology, University College London

⁴:Donders Institute for Brain Cognition and Behaviour, Radboud University

Abstract

The majority of cortical synapses are local and excitatory. Local recurrent circuits could implement amplification, allowing for pattern completion and other computations¹⁻⁴. Cortical circuits contain subnetworks, consisting of neurons with similar receptive fields and elevated connectivity relative to the network average^{5,6}. Cortical neurons encoding different types of information are spatially intermingled and distributed over large brain volumes⁵⁻⁷, hampering experiments that probe the function of these subnetwork by perturbing them individually⁸. We used computational modeling, optical recordings and manipulations to probe the function of recurrent coupling in layer (L) 2/3 of vibrissal somatosensory cortex during active tactile discrimination. A neural circuit model of L2/3 revealed that recurrent excitation enhances sensory signals via amplification, but only for subnetworks with elevated connectivity. Model networks with high amplification were sensitive to damage: loss of a few subnetwork members degraded stimulus encoding. We tested this prediction by mapping neuronal selectivity⁷ and photoablating^{9,10} neurons with specific selectivity. In L2/3 of the somatosensory cortex, ablating a small proportion (10-20, < 5 % of the total) of neurons representing touch dramatically reduced responses in the spared touch representation, but not other representations. Ablations most strongly impacted neurons with stimulus responses similar to the ablated population, also consistent with network models. Recurrence among cortical neurons with similar selectivity therefore drives input-specific amplification during behavior.

Two circuit motifs contribute to neural dynamics in cortical layer (L) 2/3: recurrent excitation, which may cause amplification^{1-5,11,12}, and feedback inhibition, which may

*:current address

Author contributions

SP and KS conceived the project. SP, RP, and TV performed the experiments, with assistance from HO. JW performed the modeling, with input from JF, SP and KS. SP, RP, TV, JW, JF, and KS analyzed data and wrote the paper.

Data and code availability

Code for the simulations can be found at <https://github.com/jwittenbach/ablation-sim>.

Code used for data analysis can be found at <https://github.com/peronlab/ablation>.

Data can be found at [CRCNS.org](https://www.crcns.org) at <http://dx.doi.org/10.6080/K0Z31WWG>.

Competing interests

The authors declare no competing interests.

account for the sparse activity typical of L2/3¹²⁻¹⁴. We explored the role of these motifs in an integrate-and-fire model of layer (L) 2/3 of the vibrissal somatosensory ('barrel') cortex constrained by measured physiological properties^{15,16} (Methods).

To model input-specific recurrent coupling, we restricted the sensory input to a subnetwork of the excitatory neurons (200 of 1,700), corresponding to the number of L2/3 barrel cortex neurons responding to active touch^{7,17} (Fig. 1a). We simulated touch-related input to L2/3 based on recordings of their L4 inputs¹⁸ (Methods). To measure the faithfulness with which neural activity reflects the sensory input, we computed an 'encoding score' (R_{stimulus}) by cross-correlating the spike rate of each neuron with the input (Methods).

We varied recurrence by changing the connection probability within the input-recipient subnetwork ('subnetwork connectivity'; synaptic conductance was scaled proportionately⁵, Methods). For each subnetwork connectivity we matched the encoding score distribution to that measured *in vivo*⁷ by adjusting the strength of the L4 input. Subnetworks with connectivity equal to and moderately elevated relative to the rest of the network (non-subnetwork connectivity, 0.2; subnetwork connectivity range, 0.2 - 0.4) produced responses consistent with those observed *in vivo*⁷ (Fig. 1b; Methods). The amplitudes of the required sensory input declined with increasing subnetwork connectivity. Amplification, defined as the ratio of network output to network input, therefore increased with subnetwork connectivity¹ (Fig. 1c). Additional elevation of subnetwork connectivity (> 0.4) produced all-or-none network responses, whereby a transient input drove the network into a persistently active state¹⁹ (Extended Data 1).

Overall, subnetwork behavior fell into three regimes, each of which produced a distinct response to removal ('ablation') of a small number of neurons. Subnetworks with low connectivity (0.2) amplified little, and were resistant to ablation (Fig. 1c-f). Encoding scores for spared neurons increased following simulated ablation of 10 % of the subnetwork¹⁴, because of reduced feedback inhibition^{13,20} (encoding score, from 0.237 ± 0.027 to 0.274 ± 0.032 , grand median \pm adjusted median absolute deviation, MAD, $P < 0.001$, Wilcoxon signed rank test, across $N = 30$ simulated networks with different randomized connectivity and initial conditions; Methods; Fig. 1d-f).

Subnetworks with elevated connectivity (e.g., 0.4) exhibited stronger amplification^{1,4} (Fig. 1c). Ablations reduced encoding scores for spared neurons, from 0.243 ± 0.049 to 0.143 ± 0.028 (connectivity = 0.4; $P < 0.001$, $N = 30$ networks), because of reduced nonlinear amplification (Fig. 1d-f). Networks in the all-or-none regime¹⁹ were robust to ablation, maintaining their response (Extended Data 1). The response of subnetworks to ablations therefore distinguishes the three regimes.

We next performed a similar analysis for actual L2/3 networks during behavior. We trained mice with a single spared whisker on an object localization task (Fig. 2a, b; Methods) and recorded neural activity with volumetric imaging⁷ in L2/3 of the barrel column corresponding to the spared whisker (Fig. 2c; $8,126 \pm 2,436$ neurons per mouse, mean \pm S.D.; $N = 16$ mice; Extended Data Table 1; Methods). Activity in a subset of neurons encoded whisker position ('whisking' neurons), whereas others responded to touch-induced

changes in whisker curvature ('touch' neurons)⁷ (Fig. 2d, e). An encoding model generated a prediction of neural activity from vibrissal kinematics (Methods). Correlating the prediction with the actual neural activity yielded an 'encoding score', which was used to assign neurons to the touch and/or the whisking representations⁷ (Methods). Across mice (N = 16 mice; Extended Data Table 1), 901 ± 539 neurons of the imaged neurons encoded touch (fraction: 0.108 ± 0.051) and 865 ± 364 encoded whisking (fraction: 0.106 ± 0.028).

We probed the roles of recurrence by ablating members of the touch representation and examining the effect on spared neurons. Multiple excitatory neurons were ablated using multiphoton excitation^{9,10} (Extended Data 2, 3). Ablating a small proportion of strong touch cells (Fig. 2f; 16.8 ± 12.8 neurons, 6 % of touch neurons in the spared whisker's barrel column, N = 9 mice; touch score, 70th \pm 35th percentile) reduced responses to touch in the spared touch neurons (Fig. 2g, h). The touch encoding score (R_{touch}) across touch neurons declined (from 0.123 ± 0.021 to 0.100 ± 0.037 , grand median \pm adjusted MAD; N = 9 mice, 8,392 neurons, P = 0.004, Wilcoxon signed rank test for animal medians, paired by animal; Fig. 2j; Methods), as did the touch neuron count (from 932 ± 634 to 716 ± 469 , mean \pm SD, calculations exclude ablated neurons, Methods). The whisking encoding score (R_{whisking}) did not change (Fig. 2i, k; from 0.116 ± 0.013 to 0.115 ± 0.024 ; 6,975 neurons, P = 0.820; neuron count: from 775 ± 267 to 721 ± 241).

In the model, more extensive ablations caused larger encoding score declines (Extended Data 4). In agreement with this prediction, the decline in touch representation increased as more of the touch representation was ablated (Fig. 2l; Pearson correlation of change in R_{touch} and net R_{touch} ablated, $R = -0.794$, P < 0.001 across all 24 ablations; $R = -0.779$, P = 0.013 for the 9 touch cell ablations). Touch neurons proximal (15-35 μm) to the ablated cells experienced a larger decline in R_{touch} than those distal (115-135 μm) from the ablated cells (Fig. 2m). The effects of ablating the touch neurons decayed over a distance ($\lambda = 87 \mu\text{m}$, exponential fit; Fig. 2m) similar to the spatial scale of local recurrent connectivity in the rodent sensory cortex²¹. Whisking neurons exhibited no distance-dependent change (Extended Data 5). The declining touch representation was not caused by changes in whisker movement or behavior (Extended Data 6). This result is consistent with amplification of touch responses by recurrent excitation in L2/3.

In contrast, ablating a subset of strong whisking neurons (12.7 ± 5.7 neurons, ~4 % of whisking neurons in the spared whisker's barrel column, N = 7 mice; whisking score: 66th \pm 37th percentile) produced no effect on either the touch (Extended Data 7, Fig. 2j; R_{touch} from 0.112 ± 0.081 to 0.095 ± 0.069 , N = 7 mice, 5,866 neurons, P = 0.109, count from 838 ± 401 to 899 ± 548) or the whisking representation (R_{whisking} from 0.108 ± 0.076 to 0.107 ± 0.076 , N = 6,161, P = 0.812, count from 880 ± 387 to 974 ± 558). Similarly, ablating silent neurons (event rate below 0.025 Hz; Methods; 16.3 ± 2.6 neurons, N = 8 mice) did not change the touch (Extended Data 7, Fig. 2k; R_{touch} from 0.115 ± 0.021 to 0.107 ± 0.023 , N = 8 mice, 7,110 neurons, P = 0.383, count from 889 ± 713 to 926 ± 681) or whisking representations (R_{whisking} from 0.115 ± 0.014 to 0.114 ± 0.015 , 7,684 neurons, P = 0.844, count from 961 ± 464 to 904 ± 384). Touch ablations produced significantly different encoding score changes among touch (but not whisking) representations than either whisking or silent ablations, whereas whisking ablations did not produce significantly different changes from silent

ablations (Fig. 2j,k). Non-specific effects of ablation therefore do not contribute to changes in the touch representation after ablation.

Whisking neuron ablations did not degrade the whisking representation. Our network model suggests that the slower kinetics of the whisking input do not account for this lack of effect, as networks having elevated subnetwork connectivity (0.4) with slower input ($t_{\text{peak}} = 50$ ms, vs. 10 ms for touch simulations; Methods) were sensitive to simulated ablation (Extended Data 8). Touch input is in-phase across the neural population^{17,18}, which engages recurrent excitation. In contrast, individual neurons encode whisking input with different phases²²; this asynchronous population response is expected to engage recurrent excitation less effectively. Therefore, the lack of sensitivity to ablation in the whisking population does not necessarily imply an absence of recurrent coupling.

In recurrent networks connected in a feature-specific manner⁵, the effects of ablation on spared neurons should increase with the similarity of their tuning to the ablated population^{23,24}. We tested this intuition in our model, defining ‘response similarity’ as the correlation of single neuron activity with the mean activity of the ablated neurons (Fig. 3a; Methods). In networks with elevated subnetwork connectivity, neurons with high response similarity showed the largest decline in encoding score following ablation (Fig. 3b). In networks without elevated subnetwork connectivity, the relationship disappeared (Fig. 3b).

We performed a similar analysis on our experimental data. Our imaging strategy sampled activity from three planes simultaneously (Fig. 2c; Methods)⁷. Because not all neurons were recorded simultaneously, it was not possible to compute a mean across ablated neurons or correlations between that mean and the activity of individual neurons. We therefore devised a ‘response similarity’ metric not requiring simultaneous recording. For each neuron, we averaged pre-ablation responses across both trial types (Fig. 3c). Concatenating these yielded a neuron’s trial-averaged F/F (Fig. 3d). Computing the mean trial-averaged F/F across all ablated neurons provided the ablated neuron mean response. Response similarity was measured for each neuron as the correlation between its trial-averaged F/F response and the mean response across all ablated neurons.

Changes in R_{touch} following ablation depended on response similarity (Fig. 3e, f). R_{touch} in neurons with high response similarity declined. Neurons with negative response similarity showed increased R_{touch} , potentially due to reduced feedback inhibition previously evoked by the ablated neurons²⁰ (Fig. 3e). Touch neuron ablation had no effect on the whisking network (Fig. 3f). Whisker neuron ablation had no effect on either representation (Fig. 3g).

Targeted photoablation allowed us to test the roles of recurrence in cortical circuits¹. The selective degradation of representations similar to the ablated neurons is consistent with amplification in recurrent networks^{1-4,11,12,23,25,26} (Fig. 1), but inconsistent with circuit models of sparse coding that are dominated by feedback inhibition^{12,14,20,27} or models with persistent activity¹⁹. Our experiments reveal that cortical circuits can be surprisingly sensitive to damage targeting specific representations, despite remarkable robustness to other kinds of perturbations²⁸.

Methods

Network model

We modeled the L2/3 network associated with a single barrel column, one of the most extensively studied cortical microcircuits^{29,30}, as a network of leaky integrate-and-fire neurons³¹. The dynamics of each neuron were governed by:

$$\tau \frac{dV_i}{dt} = V_r - V(t) + R [I_i^{exc}(t) + I_i^{inh}(t) + I_i^{ext}(t)]. \quad (1)$$

Here, V is the membrane potential, V_r is the rest/reset potential, τ is the membrane time constant, R is the input resistance, I^{exc} and I^{inh} are excitatory and inhibitory synaptic currents, I^{ext} is a current representing sensory stimulus drive (e.g. from layer 4 inputs), and i indexes the neurons in the network. When the membrane potential reaches the spiking threshold, V_{th} , a spike is emitted, the membrane potential is reset to V_r , and the dynamics of the neuron are frozen for a short refractory period, t_{ref} . The synaptic currents follow kick-and-decay dynamics:

$$\tau_{syn} \frac{dI_i^{syn}}{dt} = -I_i^{syn} + \tau_{syn} \sum_{j,k} w_{ij} \delta(t - t_i^{syn} - t_d). \quad (2)$$

In this equation, syn denotes the type of synapse (either exc or inh), τ_{syn} is the synaptic time constant, w_{ij} is a matrix of synaptic strengths from neuron j to neuron i , t_{jk} is the time of the k^{th} spike of neuron j , and t_d is the spike transmission delay. The sum over j is over all neurons, while the sum over k is over all spikes from that neuron.

The network comprised 2,000 neurons, of which 1,700 (85%) were excitatory and 300 (15%) were inhibitory¹⁶. Excitatory neurons had $\tau = 30$ ms, whereas inhibitory neurons had faster dynamics with $\tau = 10$ ms^{15,16}. As the subthreshold dynamics for these neurons are linear, the behavior of these neurons is invariant to changes of scale in V . The meaningful quantity is $V = V_{th} - V_r$ which we assume to be, on average, 35 mV for all neurons^{15,16}. Each neuron was assigned a value chosen uniformly within a range of $\pm 50\%$ of this mean value. Excitatory and inhibitory post-synaptic currents (PSCs) had time constants of $\tau_{exc} = 2$ ms and $\tau_{inh} = 3$ ms, respectively. The refractory period for spiking was $t_{ref} = 0.5$ ms. Synapses had a mean synaptic delay of $t_d = 0.6$ ms¹⁵; each individual synapse was assigned a value chosen within a range of $\pm 50\%$ of this mean value. Although all neural parameters could be modeled as random variables, we found that jittering V for the neurons and t_d for the synapses provided sufficient heterogeneity to give a broad range of baseline spike rates across neurons and also prevented network synchronization. The input resistance, R , was factored into the synaptic weights and the magnitudes of the external currents, as described below.

The excitatory population was subdivided into two groups: a small input-recipient subnetwork of 200 neurons and the remainder of the excitatory population (1,500 neurons).

Although all neurons in L2/3 likely receive touch-related input from L4³², only a small proportion are driven to spike after touch^{7,17}, justifying this model assumption. We neglected feedforward inhibition³³. This is justified because feedforward inhibition simply rescales input from L4², which in our model is adjusted to produce experimental observed population activity levels. Thus, each neuron belonged to one of three groups: the excitatory subnetwork (S), the remainder of the excitatory population (E), or the inhibitory population (I). Connections between neurons are determined by a block stochastic model. Given two neurons – the first from group A, the second from group B – there was a fixed probability of a connection from the first neuron to the second, denoted p_{AB} .

In our ‘equal subnetwork connectivity’ network, we employed sparse connectivity between excitatory neurons, $p_{SS} = p_{SE} = p_{ES} = p_{EE} = 0.2$, and more dense connectivity both within the inhibitory population as well as between the excitatory and inhibitory populations, $p_{II} = p_{IS} = p_{IE} = p_{SI} = p_{EI} = 0.6$ ^{15,16}. All connections had the same strength, which was chosen so that the resulting post-synaptic potential (PSP) is 1 mV^{15,16}. Because it is the only connectivity parameter that was varied systematically, we denote p_{SS} as P_{conn} in the rest of the text.

In the ‘elevated subnetwork connectivity’ version of the network, P_{conn} was increased to 0.4. To replicate the experimentally observed relationship between connectivity and synaptic strength⁵, the synaptic weight for these connections was increased to give PSPs of 1.6 mV. Networks with other levels of connectivity within the subnetwork were produced by linear interpolation/extrapolation of both P_{conn} and synaptic strength between the ‘equal subnetwork connectivity’ and ‘elevated subnetwork connectivity’ cases.

The stimulus drive to the network was modeled as an external current targeting the excitatory subnetwork (group S; $I^{ext} = 0$ for all neurons in groups E and I). For each stimulus presentation, the waveform of the current was modeled with a beta distribution with shape parameters $\alpha = 3$ and $\beta = 5$. The beta distribution is defined on the interval $[0, 1]$, giving a distinct beginning and end to the stimulus. For the chosen shape parameters, the beta distribution has a value of 0 at its endpoints and a peak at $(\alpha-1)/(\alpha+\beta-2)$. To model the fast touch stimulus, the waveform was stretched in time so that the peak occurs 10 ms after the start (full width half-max, 12.8 ms)¹⁸. The amplitude of the stimulus waveform was chosen so that the network response matched the experimental data. All neurons also receive tonic background input in the form of a Poisson spike train of excitatory spikes with a frequency of 5,000 Hz for excitatory neurons and 2,000 Hz for inhibitory neurons; these values were selected so that the tonic firing rate of these populations were ~0.5 Hz for excitatory neurons and ~10 Hz for inhibitory neurons³⁴⁻³⁶.

Simulations were performed in Python using the Brian2 simulation package³⁷ with a step-size of $dt = 0.1$ ms. For each randomly sampled network connectivity, the network was first simulated for 20 s of model time (corresponding to 66 stimulus presentations) and spike trains for all neurons were recorded. The activity of each neuron was then given an encoding score, which quantifies the signal-to-noise ratio of the representation of the stimulus: the neuron’s spike train was convolved with a Gaussian kernel (standard deviation, 20 ms) to produce a firing rate; the firing rate as well as the stimulus waveform was down-sampled by

a factor of 5 (to a sample period of 0.5 ms) and the normalized cross-correlation between the signals was computed for leads/lags up to 10 ms; the peak value this cross-correlation is the encoding score.

We first ran exploratory simulations to constrain the strength of the input to the subnetwork to match physiological data⁷. We simulated both the ‘equal subnetwork connectivity’ ($P_{conn} = 0.2$) and the ‘elevated subnetwork connectivity’ ($P_{conn} = 0.4$) networks across a range on sensory input strengths. In both cases, we examined the distributions of excitatory neuron encoding scores as a function of input strengths, selecting the input strength that produced a distribution most closely matching the experimental data (in terms of distribution shape and fraction of neurons encoding the stimulus). With input strengths defined for these two cases, we then used linear interpolation/extrapolation to select the input strength for other amounts of subnetwork connectivity. Because this procedure ensured a fixed network output following the simulated sensory stimulus, amplification (ratio of network output to sensory input; Fig. 1c) was defined as the inverse of the sensory input strength². Amplification was normalized to the case where neurons within the input-recipient subnetwork had connectivity probabilities equal to the non-input recipient excitatory population (that is, $P_{conn} = 0.2$).

The final set of simulations explored the effects of targeted ablation across a range of subnetwork connectivity levels (Figs. 1,3, Extended Data 1), number of ablations (Extended Data 4), and input kinetics (Extended Data 8). To simulate targeted ablation, we employed 30 randomized network instances for each subnetwork connectivity level, number of ablations, and input rise time, and calculated the pre-ablation encoding score for each neuron. The 20 excitatory neurons with the highest encoding score were then removed (all outgoing synaptic strengths set to 0), the simulation was repeated, and the post-ablation encoding scores were computed. Examination of the effects of the number of ablated neurons was done with the top 0, 10, 20, 50 and 100 neurons (Extended Data 4). This was repeated for 30 different realizations of the stochastic network connectivity. Neurons were considered to be part of the sensory input representation if they had an encoding score above 0.1; the effect of the ablation (Fig. 1e, f) was quantified as the change in encoding score across all neurons that met the 0.1 encoding score criteria either before and/or after ablations. The response similarity analysis (Fig. 3) used a more stringent encoding score cutoff of 0.25; using a cutoff of 0.1 did not alter the result, but reduced the magnitude of the observed effect. The ablated neurons were excluded for both pre- and post-ablation encoding score distribution calculations, as well as in constructing peristimulus time histograms (Fig. 1b,e).

In modeling the effect of the number of neurons ablated on the change in encoding score (Extended Data 4), we restricted our modeling to the elevated subnetwork connectivity case, $P_{conn} = 0.4$. For simulations of ‘whisking’ input (Extended Data 8), we shifted from a ‘touch’-like stimulus, peaking 10 ms after stimulus onset, to one peaking 50 ms after onset to mimic the response to whisking input observed *in vivo*^{17,18,22,35}. We examined both the equal ($P_{conn} = 0.2$) and elevated ($P_{conn} = 0.4$) connectivity cases.

For large subnetwork connectivity ($P_{conn} > 0.4$), the network transitioned to all-or-none behavior, where strong enough input can drive the subnetwork into a state of persistent elevated firing (Extended Data 1)¹⁹. To reset the network after such a transition, we introduced a strong pulse of excitatory current to the inhibitory population 300 milliseconds after the stimulus onset. In this regime the extrapolation scheme for setting the stimulus strength did not apply, since spike rate was dictated by network properties and not the input strength. Instead, the input strength affected the reliability with which a stimulus would cause a transition to the state of elevated firing. We found that choosing a stimulus strength of twice what our extrapolation scheme dictated produced a reasonable number of stimulus-encoding neurons. Thus, we used this criterion to set the input strength in this regime.

Peri-stimulus time histograms (PSTHs) were constructed by averaging the Gaussian-convolved (kernel standard deviation, 20 ms) responses of individual neurons, aligned to the sensory input.

Determining model synaptic weights

Model synapses were defined by kick-and-decay dynamics of the post-synaptic currents. We set the synaptic weights to produce a desired amplitude of the resulting unitary post-synaptic potential (PSP). Here, we derive the relationship between the synaptic weight and the PSP size that allows us to do this.

Assume that a synaptic current starts at $I = 0$ when a single spike of weight w arrives at $t = 0$. In the absence of any other spikes, the subsequent time-course of the current is found by integrating (2):

$$I(t) = we^{-t/\tau_{syn}}. \quad (3)$$

To determine the resulting behavior of $V(t)$, make the assumption that the PSP evolves according to a difference of exponentials:

$$V(t) = V_0(e^{-t/\tau_1} - e^{-t/\tau_2}). \quad (4)$$

Differentiating (4) and using (3), one can show that this form does indeed solve (3) if we choose:

$$\tau_1 = \tau_m, \tau_2 = \tau_{syn}, \text{ and } V_0 = \frac{Rw}{\tau_m/\tau_s - 1}. \quad (5)$$

The PSP size is the maximum value of $V(t)$, which we can compute as:

$$V_{max} = V_0 a^{(1-a^{-1})^{-1}} (a-1), \quad (6)$$

where $a = \tau_m/\tau_s$ is the ratio of the time constants. Comparing this to the expression for V_0 in (6) we find our desired relationship:

$$Rw = V_{max}a^{(1-a^{-1})^{-1}}. \quad (7)$$

The linearity of the synaptic dynamics allows us to use (7) to avoid explicitly determining the value of R .

Animals

All procedures were performed in compliance with the Janelia Research Campus Institutional Animal Care and Use Committee and the New York University University Animal Welfare Committee. Two transgenic lines were used for these experiments, differentiated in Extended Data Table 1 by a 'j' or 'n' in Animal ID. Animals whose ID starts with the letter 'j' consisted of mice expressing nuclear localized mCherry in a Cre-dependent manner (R26-LSL-H2B-mCherry⁷; JAX 023139) crossed with mice expressing Cre in cortical pyramidal neurons (Emx1-IRES-Cre³⁸; JAX 005628). In cortical L2/3, these animals expressed nuclear mCherry only in nuclei of excitatory neurons. Multiple (9 or 12) injections (450 μ m deep, 300 μ m apart; beveled pipettes, World Precision Instruments; 20 nL each, at 10 nL/min with a custom-built microinjector) of AAV2/1-syn-GCaMP6s (UPenn AV-1-PV2824)³⁹ were made in barrel cortex (3.6 mm lateral, 1.5 mm posterior) of young adult mice⁷ (6-8 week). Following viral injection, a titanium headbar was attached to the skull and the craniotomy was covered with a cranial window. Craniotomies were always over the left hemisphere. Animals whose ID starts with the letter 'n' consisted of mice expressing GCaMP6s in a Cre-dependent manner (Ai162⁴⁰, JAX 031562), crossed with Slc17a7-IRES2-Cre⁴⁰ (JAX 023527) to restrict expression to in pyramidal neurons. Surgeries for these animals did not include viral injections but were otherwise identical.

Behavior

Approximately one week after surgery, mice were trimmed to a single row of whiskers (typically the C row) and placed on water restriction⁴¹ (1 mL per day). Training commenced 5-7 days after restriction onset. Animals were trained on an object localization task (Fig. 2a, b)^{42,43}. If the pole appeared in a range of proximal positions, the animal would be rewarded with a small water drop for licking the right lickport; pole presentation at the distal position would be rewarded upon licking the left lickport (Fig. 2a). Trials consisted of a 1-1.2 s sample epoch followed by a 0.5-1.2 s delay epoch after which a 50 or 100 ms 3.4 kHz auditory response cue signaled to the animal to respond (Fig. 2b). To prevent premature licking, the lickport was brought into tongue range by a motor (Zaber) only during the response epoch (Fig. 2b). Mice exhibiting excessive premature licking (licks before reward cue on >20% of trials; licks monitored with a laser beam; Thorlabs) were not used.

Mice were trimmed to a single whisker after reaching criterion performance ($d' > 1.5$ for two consecutive days). The spared whisker barrel column was identified using the neuropil signal, as described previously⁷. Whisker videography was performed at 400-500 Hz. Whiskers were tracked using an automated software pipeline⁴⁴ and then curated using custom browser software⁷.

Mice were assigned randomly to experimental groups (ablation type). Experimenters were not blind to the group.

Imaging

Calcium imaging was performed using a custom two-photon microscope (<http://openwiki.janelia.org/wiki/display/shareddesigns/MIMMS>) with a 16X, 0.8 NA objective (Nikon)⁷. GCaMP (BG22; Chroma) and mCherry (675/70 filter; Chroma) fluorescence was imaged using GaAsP PMTs (Hamamatsu). The 940 or 1000 nm (Coherent) imaging beam was steered with a 16 kHz line rate resonant galvanometer (Thorlabs); a piezo collar (Physik Instrumente) moved the focus axially. 512 x 512 pixel images were collected at 7 Hz, with three 600 x 600 μm images per piezo cycle. Planes were spaced 15 μm apart. Scanimage⁴⁵ (Vidrio Technologies, <http://www.vidriotech.com>) controlled the microscope. Three planes, constituting a ‘subvolume’, were imaged simultaneously (4-6 subvolumes, spanning 45 μm each, 12-18 total planes, 180-270 μm in depth total), and power was modulated with depth using a length constant of 250 μm . Deeper subvolumes were typically imaged with higher power, using a similar length constant. Individual subvolumes were typically imaged for 50 trials per day, with all subvolumes usually visited on any given day. Alignment across days was performed as described previously^{7,46}.

Imaging data were processed using a semi-automated software pipeline that included image registration, segmentation, neuropil subtraction, F/F computation, and event detection⁷. The de-noised F/F trace, which consisted of the event amplitude trace convolved with event-specific exponential rise and decay, was used for analysis.

Neuronal classification

Neurons were classified using a linear-nonlinear encoding model^{7,47}. The model consisted of a cascaded generalized linear model that used a temporal and stimulus domain kernel to predict the activity of individual neurons given whisker angle, θ , or whisker curvature, κ , assuming Gaussian noise with input nonlinearities.

The model predicted the neuronal response, r (i.e., F/F), as

$$\begin{aligned} r &\sim \text{Norm}(z, \sigma^2) \\ z &= f_1(s_1) * k_1 + f_2(s_2) * k_2 \end{aligned}$$

Here, s_1 and s_2 are the whisker angle, θ , and whisker curvature, κ , respectively. The terms f_1 and f_2 are static, point-wise nonlinearities comprising a weighted sum of sixteen triangular basis functions

$$f = \sum_{i=1}^{16} w_i b_i(x)$$

Where x is the input (s_1 or s_2), with each b_i given by

$$b_i = \begin{cases} (x - x_i - 1) / (x_i - x_i - 1), i > 1, x_i - 1 < x < x_i \\ (x_i + 1 - x) / (x_i + 1 - x_i), i < N, x_i \leq x < x_i + 1 \\ 0, otherwise \end{cases}$$

k_1 and k_2 are temporal kernels consisting of 14 time points (2 seconds).

Thus, the model gives a z-scored prediction of neural activity, z , by fitting parameters k_1, k_2, f_1, f_2 for given whisker kinematic parameters, s_1 and s_2 .

The model parameters k_1, k_2, f_1, f_2 were fit using maximum likelihood with block coordinate descent. This procedure reliably estimated model parameters within three to five iterations.

To avoid degeneracy associated with arbitrary scaling factors on either the kernels or the nonlinearities, the nonlinearities were forced to have minimum of 0 and maximum of 1. Temporal kernels were unconstrained.

A prior was used to ensure smoothness of both the temporal kernels and the nonlinearities and prevent over-fitting. Specifically, the prior added a factor to the objective function penalizing excessive second derivatives of the temporal kernels and nonlinearities. Employing such a prior corresponds to maximizing the log-posterior, with the prior adding a small penalty to the objective function. In order to fit several thousand cells efficiently, the scale factor associated with this penalty was determined from a cross-validated inspection of a random subset of neurons.

The model was fit using five-fold cross-validation across trials. That is, a randomly selected 80% of trials were used for fitting, and 20% were used for evaluation, with 5 distinct evaluation groups per fit ensuring all data was used for fitting in exactly one case. The Pearson correlation between the predicted and actual $\Delta F/F$ yielded a measure of the quality of the model fit. This correlation was used as the encoding score for barrel cortex data: R_{touch} , based on $\Delta F/F$ for touch, and R_{whisking} , based on whisker θ for whisking (Fig. 2d,e). A neuron was considered part of a representation if R_{touch} or R_{whisking} exceeded 0.1 and if the neuron's score was above the 99th percentile of scores measured from matched shuffled neural activity. These criteria are more stringent than those employed previously⁷, because ablation predominantly impacted neurons with high encoding scores. Using a less stringent criterion did not change the underlying conclusions, but did dilute the magnitude of the effect. For the response similarity analysis (Fig. 3), a threshold of 0.25 was used for the encoding score.

Shuffled activity was generated by randomizing the timing of the calcium events to construct a novel de-noised $\Delta F/F$ trace. Matched shuffled activity was selected by using neurons from the same imaging subvolume (i.e., concurrently imaged to ensure identical animal behavior) sharing a similar event rate. Event rates were matched by partitioning the neurons from a subvolume into 10 equally sized bins (in terms of neuron count). Thus, in addition to the aforementioned encoding score threshold, a given neuron's R had to exceed the 99th

percentile of R's obtained across neurons in the same subvolume and event rate bin whose event times were shuffled.

We examined robustness by partitioning individual days into two interdigitated pseudo-sessions, and measuring the correlation between encoding scores for the two pseudo-sessions⁷. The resulting correlations ranged between ~0.5-0.75. Neural classification (whisking and touch) was stable across days for trained mice. Furthermore, the touch neuron curvature kernels assumed 'V' or 'L'-like shapes⁷, meaning that high magnitude curvature changes drove the largest responses, a result consistent with the known responses of these neurons. Finally, the kernels were stable across days⁷. Thus, changes in barrel cortex encoding following ablation are not a reflection of the variability inherent to the encoding model, but rather reflect genuine changes in the underlying representations.

Ablated neurons were always excluded from analysis of experimental data, including calculations of pre-ablation population encoding scores. Analyses involving 'pre-ablation' and 'post-ablation' data were pooled across multiple behavioral sessions. Pre- and post-ablation data each consisted of at least 2 (but typically 3) behavioral sessions, with each subvolume sampled on most sessions. Given that a single subvolume was imaged for around 50 trials in a session, classification typically employed around 150 behavioral trials per neuron (minimum for encoding model: 100 trials). Neurons participating in both representations in a given area were excluded from analysis. In all cases where comparisons of pre- and post-ablation distributions were made, neurons were included for analysis if they met the criteria for representation membership (described above) in the pre- or post-ablation period, or during both periods.

Multiphoton ablation

Ablations^{9,48,49} were performed with 880 nm (Chameleon Ultra 2; Coherent) or 1040 nm (Fidelity HP; Coherent) femtosecond laser pulses delivered through a 0.8 NA, 16 X objective (Nikon) in animals that were awake but not performing the task or lightly anesthetized using isoflurane (1-2%). On the day of ablation, a new image was acquired and a warp field transform was employed to find the target neurons⁴⁶. Imaging was not performed on the day of ablation; post-ablation analyses used the imaging data from the 2-4 behavioral sessions on the days following ablation. Typically, experiments consisted of three days of pre-ablation data collection, the ablation day, and three days of post-ablation data collection.

In virally transfected mice, the mCherry signal was used to restrict ablations to pyramidal neurons⁷; in mice endogenously expressing GCaMP, presence of fluorophore was used for this purpose. The neurons with strongest touch or whisking encoding scores within the spared barrel column were targeted for ablation. The percentage of touch and whisking neurons ablated was calculated in relation to the estimated 1,691 pyramidal neurons in L2/3¹⁶, of which 17% (287) belonged to each representation⁷. Neurons participating in both representations (touch and whisking) were avoided. For silent cell ablation, neurons with a calcium event rate below 0.025 Hz were targeted for ablation.

In all cases, approximately 2/3 of ablations were successful (Extended Data 2c). Proximity to vasculature, low baseline fluorescence, and excessive depth accounted for most failures. Thus, despite targeting the strongest neurons in a given representation, the actual representation strength of ablated neurons varied. The encoding score percentile of the ablated neurons is therefore reported in the text.

After ablation we consistently observed an increase in GCaMP6 fluorescence in the targeted neuron (Extended Data 2a,b). Taking advantage of this signature, the ablation protocol consisted of interleaved ‘ablation’ and ‘evaluation’ epochs (Extended Data 2b; ablation duration: 50-200 ms; evaluation: 0.1-2 s, with longer evaluation times proving more reliable). Ablation epoch power started at the evaluation epoch power (25-100 mW, measured at the specimen) and rose linearly as necessary (up to 1W) over the course of several seconds. The beam was focused on the brightest part of the targeted neuron using a pair of galvanometers (Cambridge Technology) and oscillated over a path spanning 1-2 μm . Evaluation epoch fluorescence data was collected using standard resonant galvanometer imaging⁷, though restricted to a single plane (~30 Hz). Ablations were terminated after observation of the fluorescence rise in the target neuron.

Consistent with similar protocols^{10,50}, ablation did not produce off-target damage: calcium event rates for neurons adjacent (10-25 μm) to ablated cells did not change following the ablation of silent neurons (Extended Data 3a), and glial immunoreactivity was confined to the site of the lesioned neuron (Extended Data 3b-d).

Typically, 10-50 ablations were performed over the course of one hour. For histological analysis (Extended Data 3b-d), perfusion was performed 24h after ablation in two Emx1-Cre X LSL-H2B-mCherry animals (9 and 28 ablations were successful in these animals, approximating typical experimental conditions). Alternating cryomicrotome (Leica) sections were exposed to antibodies for either the microglial marker *iba1* (Abcam, ab5076) or the astrocytic marker GFAP (Abcam, ab7260). Glial reactions were measured by first locating the ablated neuron’s center in the glial immunoreaction image. An edge detection algorithm³⁹ that operated on an intensity image in angle-distance space from the neuron center detected the reaction’s extent (Extended Data 3d). Specifically, intensity profiles were measured across a range of angles emanating from the point within the ablation. To delimit the glial reaction, large drops in intensity were detected. Glia was considered reactive if the intensity inside the detected reaction area was two standard deviations above background image intensity.

Following ablation, nearby neurons retained sensory responses (Fig. 2f), event rate (Extended Data 3a), and maintained structural integrity (Extended Data 3b,c,e). In a few instances (N = 5) the ablation termination protocol failed, resulting in more extensive lesions (Extended Data 3f). These experiments were excluded from the study.

We excluded ablated neurons as well as neurons within a cylinder centered on ablated neurons having a radius of 10 μm and a height of 60 μm from all analyses. This excluded neurons abutting ablated cells, and ensured no neurons within a typical glial reaction radius would be included.

Response similarity

For simulated data, response similarity was measured by taking the Pearson correlation of the Gaussian-convolved (kernel standard deviation, 20 ms) activity of an individual neuron with the mean Gaussian-convolved activity of the ablated neurons (Fig. 3a). For experimental data, response similarity was measured by correlating the individual neuronal trial averaged $\Delta F/F$ to the ablated neuron trial average mean. For each neuron, trial averaged $\Delta F/F$ was calculated by taking the mean $\Delta F/F$ across all correct proximal and distal pole trials (Fig. 3c), then concatenating these two vectors (Fig. 3d). The mean of these vectors across the ablated neurons constituted the ‘ablated neuron mean’ (Fig. 3d). Response similarity is simply the Pearson correlation of the individual neuron trial averaged $\Delta F/F$ with the mean trial averaged $\Delta F/F$ across all ablated neurons. Single-network (Fig. 3b) or animal (Figs. 3e, f, g) averages were computed with response similarity bins having a width of 0.1. The grand mean of these is shown as a dark line on these plots. Only strongly responding neurons (encoding score > 0.25) were considered in this analysis (other analyses use a cutoff of 0.1).

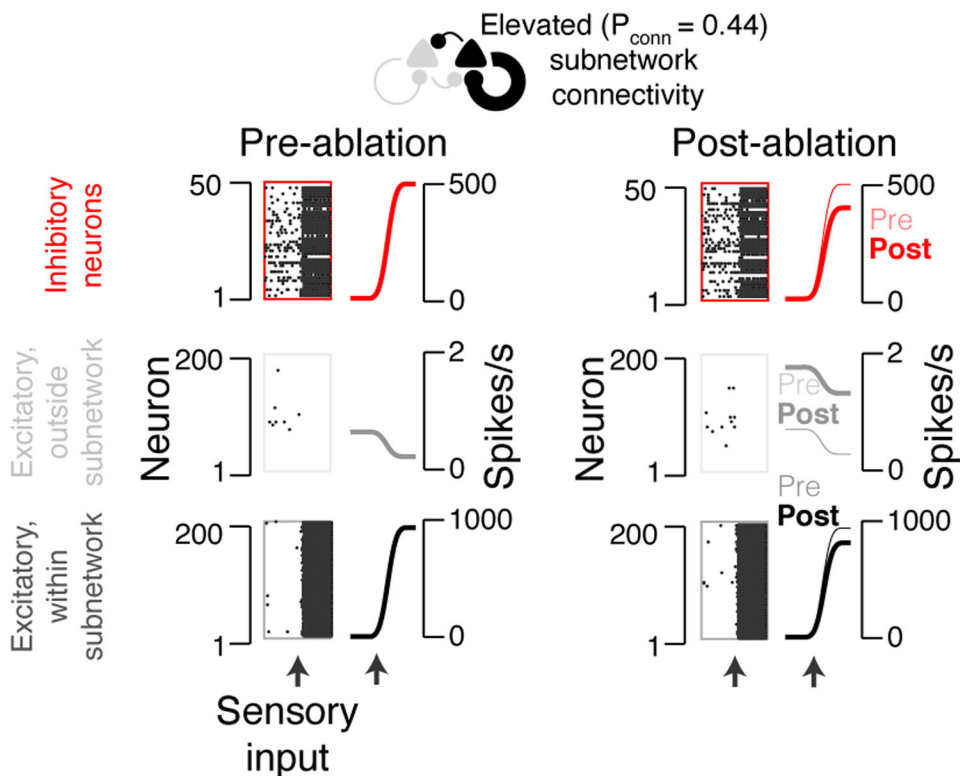
Trial-averaged $\Delta F/F$ correlations were employed instead of raw activity correlations because neurons were not all imaged simultaneously; only neurons in a given subvolume were imaged simultaneously. Because ablated neurons came from multiple subvolumes, response similarity had to employ trial-averaged responses to allow for comparison across disjointly recorded populations.

Statistical analyses

The majority of statistical comparisons were performed using the Wilcoxon signed rank test comparing paired medians within individual animals for two conditions (e.g., before and after ablation, or proximal and distal encoding score change). For cases where values had no natural pairing (comparison of different ablation types), the Wilcoxon rank sum test comparing medians was used to compare distributions. To test if encoding score change depended on response similarity (Fig. 3), we first fit a line to individual networks or animals (e.g., Fig. 3e; the linear fit is distinct from the cross-cell mean that is shown). Next, we tested whether the slopes thus obtained were distinct from 0 across all networks or animals using the non-parametric sign test.

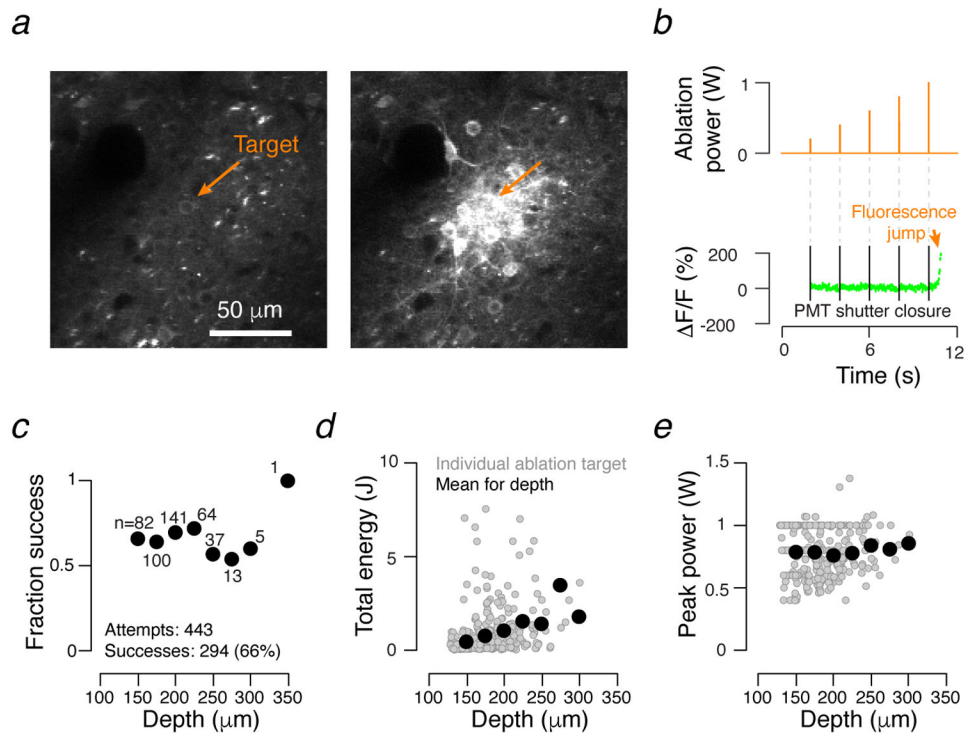
In all cases, we used the median of single-neuron values within an animal. That is, we treated mice, and never neurons, as independent observations. Where relevant, the total number of neurons included across all mice was given. Where given, adjusted median absolute deviation (M.A.D.) was calculated by multiplying the median absolute deviation by 1.4826 so as to approximate the standard deviation under conditions of normality. Sample sizes were similar to those used by others in the field. No statistical tests were used to determine sample sizes.

Extended Data



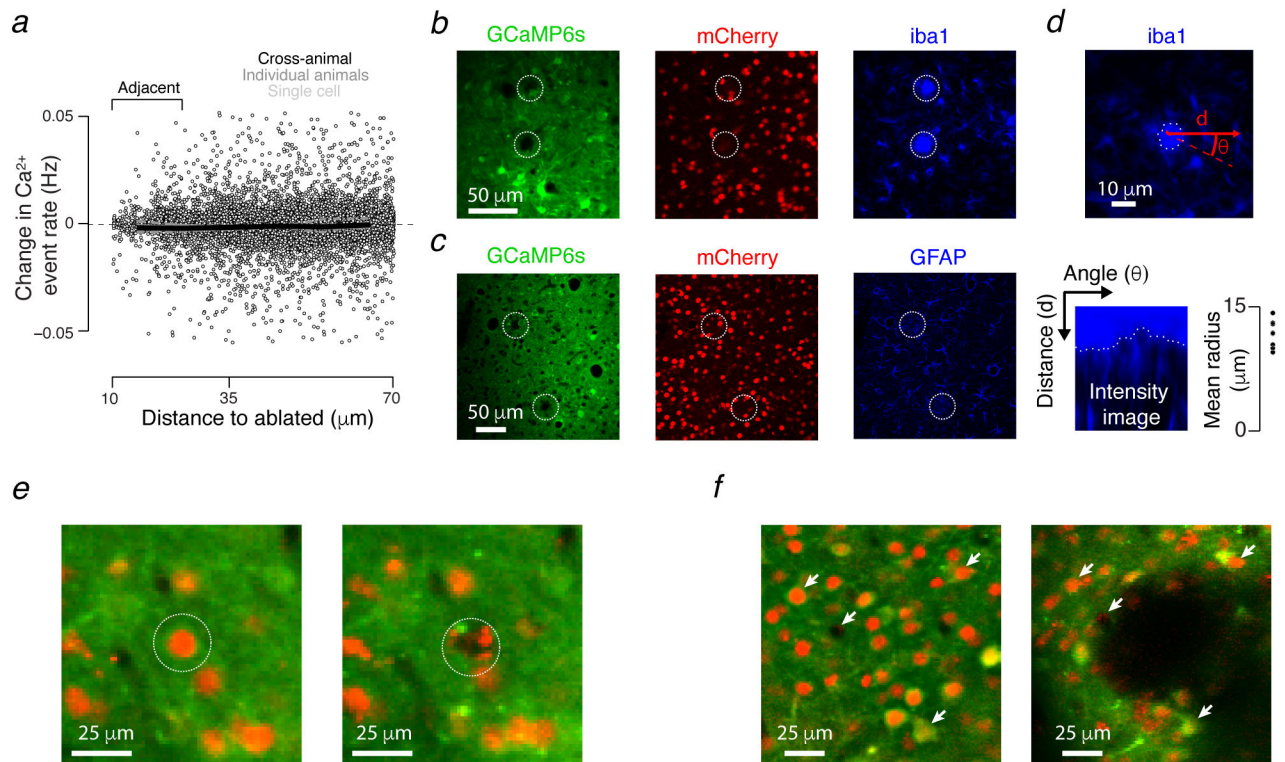
Extended Data 1.

Effect of ablation in a simulated network with hyper-connectivity (i.e., $P_{\text{conn}} > 0.4$; here, $P_{\text{conn}} = 0.44$). Model network responses aligned to input (arrow, bottom). Raster plots show a subset of neurons from an example network. Peri-stimulus time histograms show averages across all neurons and networks. Bottom, excitatory neurons within subnetwork; middle, excitatory neurons outside subnetwork; top, inhibitory neurons. Left, network response before ablation of 10% of the subnetwork neurons; right, response after ablation.



Extended Data 2.

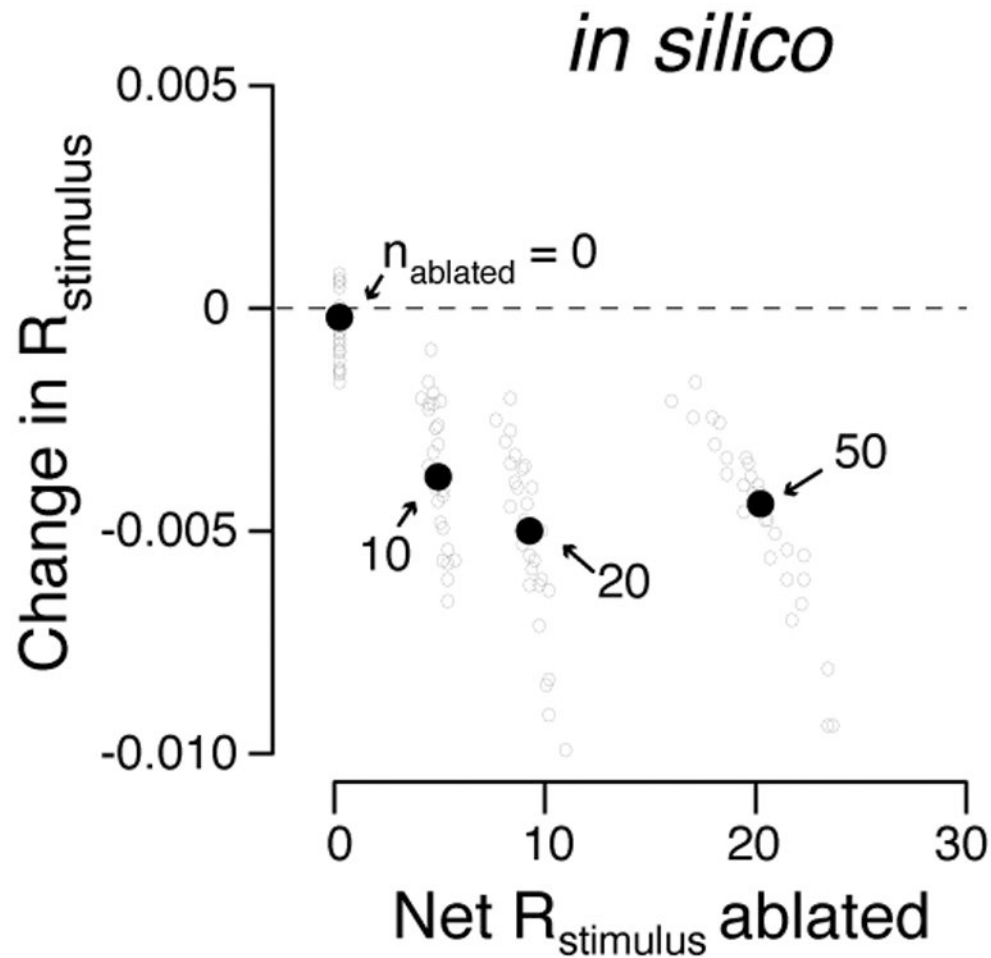
Multi-photon ablation protocol. **a.** Example field of view immediately before (left) and after (right) an ablation. Orange arrow, target neuron. **b.** Ablation protocol. Power (orange, top trace) during ablation epochs (100 ms; elevated power, orange, top) gradually increased, and the PMT shutter was closed (black bars). During the intervening evaluation epochs, power was lower and constant (orange, top), and the PMT shutter was open. Ablation was terminated when GCaMP fluorescence at the target neuron (green) jumped (orange arrow). **c.** Success of ablation as a function of neuron depth for all experiments included in this dataset. Individual points give mean success rate for given depth bin; bin size, 25 μm . **d.** Depth dependence of total energy deposition for successful ablations (successfully ablated cells only: $N = 293$ cells across 22 sessions, 14 animals; ablations from j250220 and j257218, along with 7 additional ablations from other animals were excluded due to incomplete logging). Grey dots, individual ablations. Black dots, means across 25 μm bins. **e.** As in **d**, but for peak power needed for ablation ($N = 293$ cells across 22 sessions, 14 animals).



Extended Data 3.

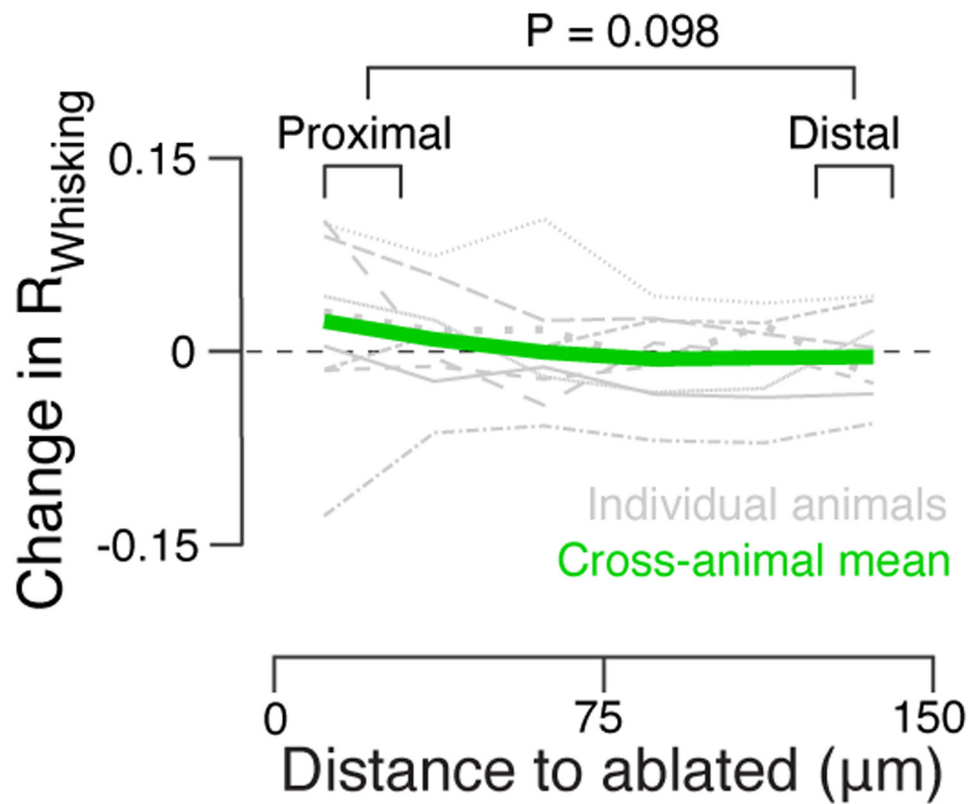
Multi-photon ablation produces spatially localized effects. **a.** Change in calcium event rate (Methods) as a function of minimal distance to an ablated neuron following silent cell ablation. Individual neurons appear as gray points, with dark gray dashed lines showing single animal averages and the dark black line showing the cross-animal ($N = 8$ silent ablation mice) average. Event rates among neurons adjacent to ablated silent cells did not change (pre-ablation event rate: 0.014 ± 0.008 Hz, grand median \pm adjusted M.A.D., Methods, post-ablation: 0.014 ± 0.007 Hz; $P = 0.055$ pre- vs. post-ablation, Wilcoxon signed rank test, paired medians across $N = 8$ mice; 1,028 neurons across all mice). **b.** Confocal *ex vivo* image from an animal perfused 24 h following ablation. Ablation sites are indicated with dashed white circles. Green, GCaMP6s fluorescence; red, mCherry fluorescence; blue, microglial antibody iba1 fluorescence. **c.** As in **b**, but blue shows immunoreactivity for the astrocytic marker, GFAP. **d.** The spatial extent of glial reaction was measured by detecting the fastest intensity decline ridge (dashed white line; Methods) in the glial antibody image along lines emanating from the ablation center at varied angles. Top, ridge along ablation from **b**. Bottom left, intensity image in angle-distance space within which the ridge was measured. Bottom right, distribution of reaction radii; all points constitute iba1 labeling, as no detectable glial reactions were observed with GFAP: 8 of 10 iba1-labeled and 0 of 6 GFAP-labeled ablations retrieved histologically revealed a detectable glial reaction (Methods). These reactions had radii of 11.7 ± 1.7 μm (mean \pm S.D.; $N = 8$ sites). **e.** Two-photon *in vivo* images before (left) and after (right) a successful ablation (target, white dotted line). Green, GCaMP6s fluorescence; red, mCherry fluorescence. **f.** As in **e**, but following a failure of the ablation protocol to terminate the ablation. Excess energy

deposition produced a large lesion (black, center of image). White arrows, corresponding points in the two images. Animals (N = 5) with such lesions were excluded from the study.

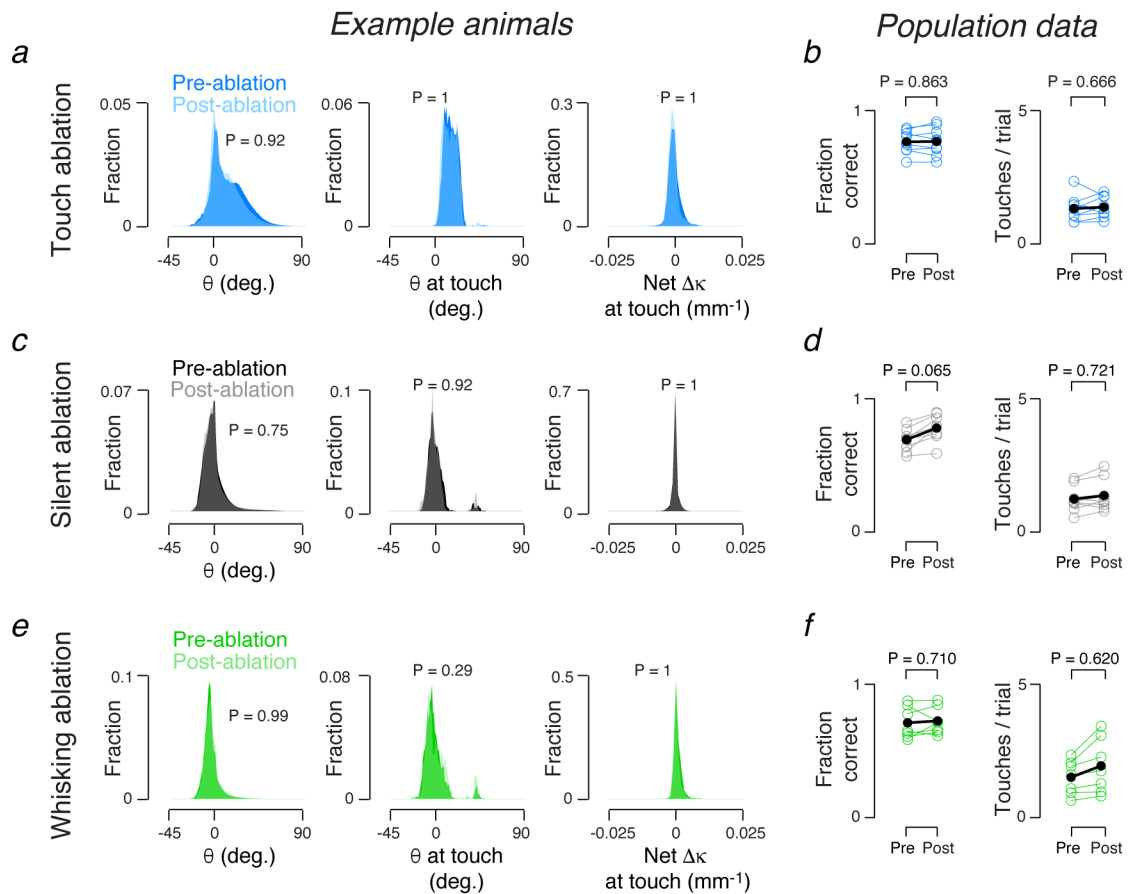


Extended Data 4.

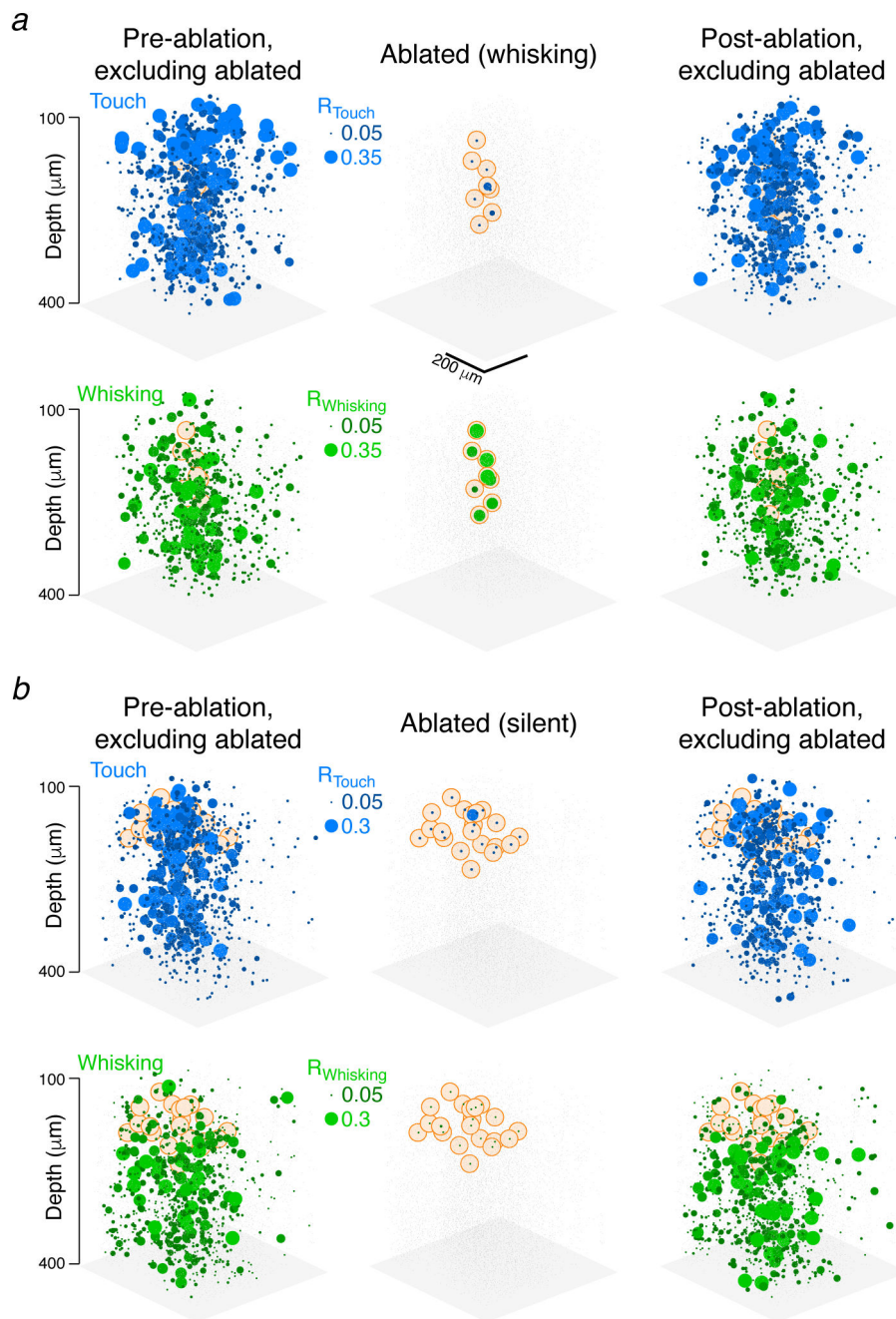
Effect of ablation on L2/3 model sensory representation increases with the number of ablated neurons. Ablation effect (change in R_{stimulus}) as a function of the degree of touch representation degradation (net R_{stimulus} across ablated neurons). In all cases, we used elevated subnetwork connectivity (0.4; Figure 1, Methods). The N_{ablated} neurons with the highest encoding score were selected for ablation. Grey circles, individual networks. Black dots, median across $N = 30$ simulated networks for a given number of ablated neurons, indicated in the plot. Beyond $N_{\text{ablated}} > 50$, we observed instability, presumably because we did not attempt to restore excitatory-inhibitory balance following ablation; these data were omitted. Correlation of net R_{stimulus} ablated and R_{stimulus} : $R = -0.65$, $P < 0.01$.

**Extended Data 5.**

Touch neuron ablation does not produce distance-dependent effects in the whisking representation. Proximal (15-35 μm to nearest ablated cell) change in P_{whisking} : 0.000 ± 0.192 (grand median \pm adjusted M.A.D.); distal (115-135 μm): -0.023 ± 0.186 , (P-value given for Wilcoxon signed rank test comparing proximal paired to distal, $N = 9$ mice); legend as in Fig. 2m.

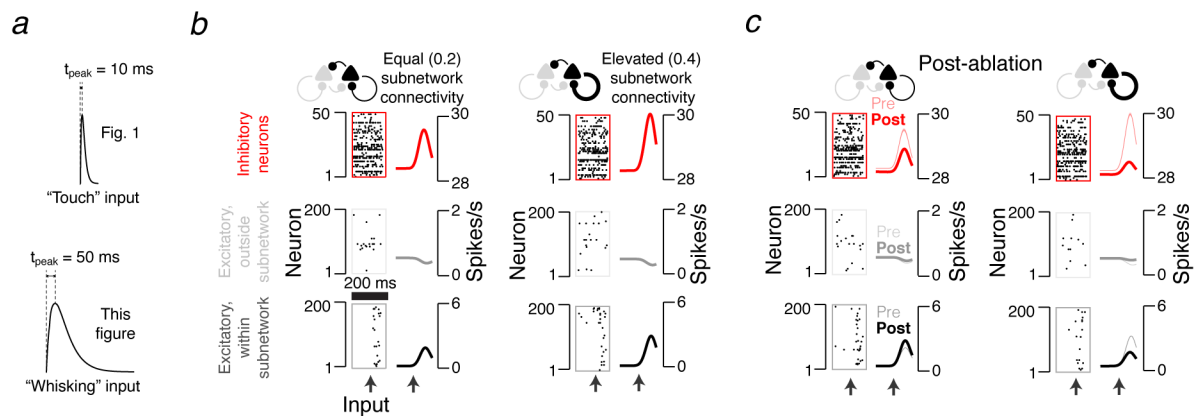
**Extended Data 6.**

Behavior does not account for ablation effects. **a.** Pre- (dark blue) and post-touch neuron ablation (light blue) distributions for whisker angle (θ), angle at touch (θ at touch), and net curvature change across all touches (net κ at touch) in an example animal. P-values, Kolmogorov-Smirnov test comparing a variable's distributions prior to and after ablation in individual mice. No animal showed a significant ($P < 0.05$) change in any of the three parameters. **b.** Fraction of correct trials (left) and number of touches (right) before and after touch neuron ablation. P-values, Wilcoxon signed rank test, paired by mouse, $N = 9$ mice. **c.** **d.** As in **a**, **b**, but for silent neuron ablations, $N = 8$ mice. **e.** **f.** As in **a**, **b**, but for whisking neuron ablations, $N = 7$ mice.



Extended Data 7.

Example effects of whisking and silent neuron ablations. **a.** Example whisking neuron ablation. Left, example maps for touch (top, blue) and whisking (bottom, green) cells before ablation. Sphere size corresponds to R_{touch} (top) or R_{whisking} (bottom). Grey dots, other neurons. These maps exclude the ablated neurons, whose position is indicated with a faint orange background. Center, R_{touch} (top) and R_{whisking} (bottom) for the ablated population. Right, R_{touch} (top) and R_{whisking} (bottom) following ablation, with ablated neurons again excluded. **b.** As in **a**, but for silent neuron ablation.



Extended Data 8.

Simulation of whisking neuron ablation produces representation degradation in networks with elevated, but not equal subnetwork connectivity. **a.** Whisking input was simulated by using input with a peak time of 50 ms (bottom), in contrast to 10 ms for touch (top; Fig. 1). **b.** Model network responses aligned to input prior to ablation. Left to right, increasing subnetwork connectivity. Bottom to top, raster plots (each showing a subset of neurons from an example network) and peristimulus time histograms (PSTHs; averaged across all neurons and networks) for the three neuronal populations in the model (Figure 1a; Methods). **c.** As in **b**, but following ablation. Thin PSTHs are before ablation. Encoding score change after ablation: from 0.143 ± 0.024 to 0.104 ± 0.013 , grand median \pm adjusted M.A.D., $P < 0.001$, Wilcoxon signed rank test paired by network, $N = 30$ networks.

Extended Data Table 1.

Individual mice are listed with the number of neurons imaged, the type(s) of ablation(s) performed, and the number of neurons ablated. The number of touch and whisking neurons is given (for the 0.1 encoding score criteria, Methods), as well as the change in median encoding score following ablation. Animals with IDs starting with a 'j' were virally transfected *Emx1-Cre X LSL-H2B-mCherry*⁷; animals with ID starting with an 'n' were *Ai162 X Slc17a7-Cre*⁴⁰.

Animal ID	Cell count	Ablated type	Ablated count	Touch count	R_{touch}	Whisking count	R_{whisking}
j250220	8,844	touch	50	867	-0.122	422	-0.076
j257218	6,215	silent	20	743	0.018	366	0.032
j257220	3,663	touch	9	389	-0.004	455	0.025
j258836	7,290	silent	16	481	0.066	666	-0.012
		touch	15	488	-0.055	655	0.001
j271211	9,415	silent	16	2,476	-0.012	551	-0.007
		touch	15	1,951	-0.061	692	0.021
j278937	4,230	silent	15	146	0.004	379	0.001
		whisking	12	150	-0.006	392	0.011
j278939	7,167	silent	20	636	-0.024	698	0.001
		whisking	13	523	-0.017	649	-0.015

Animal ID	Cell count	Ablated type	Ablated count	Touch count	R_{touch}	Whisking count	R_{whisking}
j281915	7,002	whisking	8	723	-0.010	550	0.004
		touch	11	601	-0.022	672	0.008
n274424	7,785	touch	17	706	-0.029	718	-0.014
n272761	6,359	touch	14	509	-0.001	410	0.000
n274577	12,173	touch	11	1,380	-0.013	657	0.004
n275801	8,354	silent	14	220	0.000	738	-0.007
		touch	9	197	-0.065	698	-0.006
n275798	11,364	silent	13	959	0.002	958	0.002
		whisking	11	972	0.008	1,037	0.011
n278288	9,314	whisking	25	969	-0.008	813	-0.006
n276013	11,659	silent	16	652	0.028	1,072	-0.001
		whisking	9	634	-0.012	968	-0.008
n278759	9,187	whisking	11	617	-0.003	526	-0.004

Acknowledgments

We thank Shaul Druckmann, Sandro Romani, Diego Gutnisky, Nuo Li, Jianing Yu, Hidehiko Inagaki, Nicholas Sofroniew, and Mike Economo for comments on the manuscript, Amy Hu for histology, and Hongkui Zeng for the Ai162 transgenic mice. Funding was provided by the Howard Hughes Medical Institute. RP was supported by NIH T32GM007308.

References:

- Douglas RJ, Koch C, Mahowald M, Martin KA & Suarez HH Recurrent excitation in neocortical circuits. *Science* 269, 981–985 (1995). [PubMed: 7638624]
- Chance FS, Nelson SB & Abbott LF Complex cells as cortically amplified simple cells. *Nat Neurosci* 2, 277–282, doi:10.1038/6381 (1999). [PubMed: 10195222]
- Christie IK, Miller P & Van Hooser SD Cortical amplification models of experience-dependent development of selective columns and response sparsification. *J Neurophysiol* 118, 874–893, doi:10.1152/jn.00177.2017 (2017). [PubMed: 28515285]
- Miller KD Canonical computations of cerebral cortex. *Curr Opin Neurobiol* 37, 75–84, doi:10.1016/j.conb.2016.01.008 (2016). [PubMed: 26868041]
- Cossell L et al. Functional organization of excitatory synaptic strength in primary visual cortex. *Nature* 518, 399–403, doi:10.1038/nature14182 (2015). [PubMed: 25652823]
- Lee WC et al. Anatomy and function of an excitatory network in the visual cortex. *Nature* 532, 370–374, doi:10.1038/nature17192 (2016). [PubMed: 27018655]
- Peron SP, Freeman J, Iyer V, Guo C & Svoboda K A Cellular Resolution Map of Barrel Cortex Activity during Tactile Behavior. *Neuron* 86, 783–799, doi:10.1016/j.neuron.2015.03.027 (2015). [PubMed: 25913859]
- Peron S & Svoboda K From cudgel to scalpel: toward precise neural control with optogenetics. *Nat Methods* 8, 30–34, doi:10.1038/nmeth.f.325 (2011). [PubMed: 21191369]
- Konig K, Becker TW, Fisher P, Riemann I & Halbhauer KJ Pulse-length dependence of cellular response to intense near-infrared laser pulses in multiphoton microscopes. *Optics Lett.* 24, 113–115 (1999).
- Vladimirov N et al. Brain-wide circuit interrogation at the cellular level guided by online analysis of neuronal function. *Nat Methods* 15, 1117–1125, doi:10.1038/s41592-018-0221-x (2018). [PubMed: 30504888]

11. Rubin DB, Van Hooser SD & Miller KD The stabilized supralinear network: a unifying circuit motif underlying multi-input integration in sensory cortex. *Neuron* 85, 402–417, doi:10.1016/j.neuron.2014.12.026 (2015). [PubMed: 25611511]
12. Harris KD & Mrsic-Flogel TD Cortical connectivity and sensory coding. *Nature* 503, 51–58, doi:10.1038/nature12654 (2013). [PubMed: 24201278]
13. Mateo C et al. In vivo optogenetic stimulation of neocortical excitatory neurons drives brain-state-dependent inhibition. *Curr Biol* 21, 1593–1602, doi:10.1016/j.cub.2011.08.028 (2011). [PubMed: 21945274]
14. Barrett DG, Deneve S & Machens CK Optimal compensation for neuron loss. *Elife* 5, doi:10.7554/eLife.12454 (2016).
15. Avermann M, Tomm C, Mateo C, Gerstner W & Petersen CC Microcircuits of excitatory and inhibitory neurons in layer 2/3 of mouse barrel cortex. *J Neurophysiol* 107, 3116–3134, doi:10.1152/jn.00917.2011 (2012). [PubMed: 22402650]
16. Lefort S, Tomm C, Floyd Sarria JC & Petersen CC The excitatory neuronal network of the C2 barrel column in mouse primary somatosensory cortex. *Neuron* 61, 301–316, doi:10.1016/j.neuron.2008.12.020 (2009). [PubMed: 19186171]
17. Crochet S, Poulet JF, Kremer Y & Petersen CC Synaptic mechanisms underlying sparse coding of active touch. *Neuron* 69, 1160–1175, doi:10.1016/j.neuron.2011.02.022 (2011). [PubMed: 21435560]
18. Hires SA, Gutnisky DA, Yu J, O'Connor DH & Svoboda K Low-noise encoding of active touch by layer 4 in the somatosensory cortex. *Elife* 4, doi:10.7554/eLife.06619 (2015).
19. Litwin-Kumar A & Doiron B Slow dynamics and high variability in balanced cortical networks with clustered connections. *Nat Neurosci* 15, 1498–1505, doi:10.1038/nn.3220 (2012). [PubMed: 23001062]
20. Chettih SN & Harvey CD Single-neuron perturbations reveal feature-specific competition in V1. *Nature* 567, 334–340, doi:10.1038/s41586-019-0997-6 (2019). [PubMed: 30842660]
21. Holmgren C, Harkany T, Svennenfors B & Zilberter Y Pyramidal cell communication within local networks in layer 2/3 of rat neocortex. *J Physiol* 551, 139–153, doi:10.1113/jphysiol.2003.044784 (2003). [PubMed: 12813147]
22. Curtis JC & Kleinfeld D Phase-to-rate transformations encode touch in cortical neurons of a scanning sensorimotor system. *Nat Neurosci* 12, 492–501 (2009). [PubMed: 19270688]
23. Marshel JH et al. Cortical layer-specific critical dynamics triggering perception. *Science* 365, doi:10.1126/science.aaw5202 (2019).
24. Carrillo-Reid L, Han S, Yang W, Akrouh A & Yuste R Controlling Visually Guided Behavior by Holographic Recalling of Cortical Ensembles. *Cell* 178, 447–457 e445, doi:10.1016/j.cell.2019.05.045 (2019). [PubMed: 31257030]
25. Lien AD & Scanziani M Tuned thalamic excitation is amplified by visual cortical circuits. *Nat Neurosci* 16, 1315–1323, doi:10.1038/nn.3488 (2013). [PubMed: 23933748]
26. Daie K, Svoboda K & Druckmann S Targeted photostimulation uncovers circuit motifs supporting short-term memory. *bioRxiv*, 623785, doi:10.1101/623785 (2019).
27. Hansel D & van Vreeswijk C The mechanism of orientation selectivity in primary visual cortex without a functional map. *J Neurosci* 32, 4049–4064, doi:10.1523/JNEUROSCI.6284-11.2012 (2012). [PubMed: 22442071]
28. Li N, Daie K, Svoboda K & Druckmann S Robust neuronal dynamics in premotor cortex during motor planning. *Nature*, doi:10.1038/nature17643 (2016).
29. Petersen CC & Crochet S Synaptic computation and sensory processing in neocortical layer 2/3. *Neuron* 78, 28–48, doi:10.1016/j.neuron.2013.03.020 (2013). [PubMed: 23583106]
30. Petersen CCH Sensorimotor processing in the rodent barrel cortex. *Nat Rev Neurosci* 20, 533–546, doi:10.1038/s41583-019-0200-y (2019). [PubMed: 31367018]
31. Brette R et al. Simulation of networks of spiking neurons: a review of tools and strategies. *J Comput Neurosci* 23, 349–398, doi:10.1007/s10827-007-0038-6 (2007). [PubMed: 17629781]
32. Bureau I, von Saint Paul F & Svoboda K Interdigitated Paralemniscal and Lemniscal Pathways in the Mouse Barrel Cortex. *PLoS Biol* 4, e382 (2006). [PubMed: 17121453]

33. Xue M, Atallah BV & Scanziani M Equalizing excitation-inhibition ratios across visual cortical neurons. *Nature* 511, 596–600, doi:10.1038/nature13321 (2014). [PubMed: 25043046]
34. Gentet LJ et al. Unique functional properties of somatostatin-expressing GABAergic neurons in mouse barrel cortex. *Nat Neurosci* 15, 607–612, doi:10.1038/nn.3051 (2012). [PubMed: 22366760]
35. Yu J, Gutnisky DA, Hires SA & Svoboda K Layer 4 fast-spiking interneurons filter thalamocortical signals during active somatosensation. *Nat Neurosci* 19, 1647–1657, doi:10.1038/nn.4412 (2016). [PubMed: 27749825]
36. Yu J, Hu H, Agmon A & Svoboda K Recruitment of GABAergic Interneurons in the Barrel Cortex during Active Tactile Behavior. *Neuron* 104, 412–427 e414, doi:10.1016/j.neuron.2019.07.027 (2019). [PubMed: 31466734]
37. Stimberg M, Brette R & Goodman DF Brian 2, an intuitive and efficient neural simulator. *Elife* 8, doi:10.7554/eLife.47314 (2019).
38. Gorski JA et al. Cortical excitatory neurons and glia, but not GABAergic neurons, are produced in the Emx1-expressing lineage. *The Journal of neuroscience : the official journal of the Society for Neuroscience* 22, 6309–6314, doi:20026564 (2002). [PubMed: 12151506]
39. Chen TW et al. Ultrasensitive fluorescent proteins for imaging neuronal activity. *Nature* 499, 295–300, doi:10.1038/nature12354 (2013). [PubMed: 23868258]
40. Daigle TL et al. A Suite of Transgenic Driver and Reporter Mouse Lines with Enhanced Brain-Cell-Type Targeting and Functionality. *Cell* 174, 465–480 e422, doi:10.1016/j.cell.2018.06.035 (2018). [PubMed: 30007418]
41. Guo ZV et al. Procedures for behavioral experiments in head-fixed mice. *PLoS One* 9, e88678, doi:10.1371/journal.pone.0088678 (2014). [PubMed: 24520413]
42. O'Connor DH et al. Vibrissa-based object localization in head-fixed mice. *J Neurosci* 30, 1947–1967, doi:10.1523/JNEUROSCI.3762-09.2010 (2010). [PubMed: 20130203]
43. Guo ZV et al. Flow of cortical activity underlying a tactile decision in mice. *Neuron* 81, 179–194, doi:10.1016/j.neuron.2013.10.020 (2014). [PubMed: 24361077]
44. Clack NG et al. Automated tracking of whiskers in videos of head fixed rodents. *PLoS Comput Biol* 8, e1002591, doi:10.1371/journal.pcbi.1002591 (2012). [PubMed: 22792058]
45. Pologruto TA, Sabatini BL & Svoboda K ScanImage: Flexible software for operating laser-scanning microscopes. *BioMedical Engineering OnLine* 2, 13 (2003). [PubMed: 12801419]
46. Huber D et al. Multiple dynamic representations in the motor cortex during sensorimotor learning. *Nature* 484, 473–478, doi:10.1038/nature11039 (2012). [PubMed: 22538608]
47. Ahrens MB, Paninski L & Sahani M Inferring input nonlinearities in neural encoding models. *Network* 19, 35–67, doi:10.1080/09548980701813936 (2008). [PubMed: 18300178]
48. Orger MB, Kampf AR, Severi KE, Bollmann JH & Engert F Control of visually guided behavior by distinct populations of spinal projection neurons. *Nat Neurosci* 11, 327–333, doi:10.1038/nn2048 (2008). [PubMed: 18264094]
49. Allegra Mascaro AL, Sacconi L & Pavone FS Multi-photon nanosurgery in live brain. *Frontiers in neuroenergetics* 2, doi:10.3389/fnene.2010.00021 (2010).
50. Canty AJ et al. In-vivo single neuron axotomy triggers axon regeneration to restore synaptic density in specific cortical circuits. *Nat Commun* 4, 2038, doi:10.1038/ncomms3038 (2013). [PubMed: 23799397]

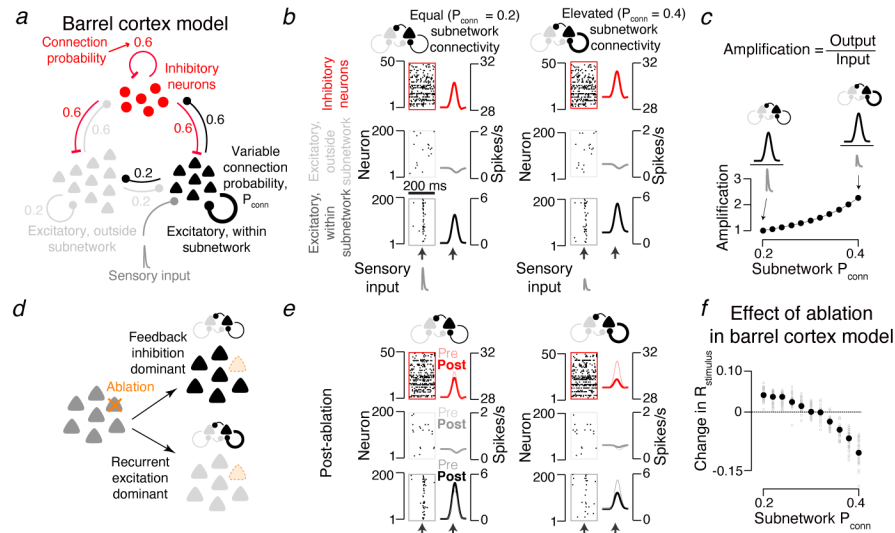


Figure 1.

Ablation effect in simulated cortical L2/3 network depends on excitatory connectivity. **a.** The L2/3 network model comprises a subnetwork of 200 excitatory neurons (black) receiving sensory input (dark grey), a larger excitatory population (1,500 neurons; light grey) without sensory input, and 300 inhibitory neurons (red). All populations are interconnected (connection probabilities listed in figure; Methods). The probability and strength of connections within the excitatory subnetwork was varied (P_{conn} , thick black loop; Methods). **b.** Model network responses aligned to input (arrows). Left, subnetwork connectivity for excitatory subnetwork equal to overall connection probability. Right, elevated connectivity. Raster plots show a subset of neurons from an example network. Peri-stimulus time histograms show averages across all neurons and networks ($N = 30$). Bottom, excitatory neurons within subnetwork; middle, excitatory neurons outside subnetwork; top, inhibitory neurons. **c.** Amplification, defined as the ratio of network output to sensory input (Methods), as a function of subnetwork connectivity, normalized to the $P_{conn} = 0.2$ case (mean across 30 networks per P_{conn}). **d.** Predicted effects of ablation. In the equal connectivity case (top), feedback inhibition dominates and responses among spared neurons increase. In the elevated connectivity case (bottom), recurrent excitation dominates and responses decline. **e.** As in **b**, but following ablation of the 20 neurons with the strongest encoding score. **f.** Effect of ablation on stimulus encoding, as a function of subnetwork connectivity. Grey circles, individual network. Black circles, mean of 30 simulated networks.

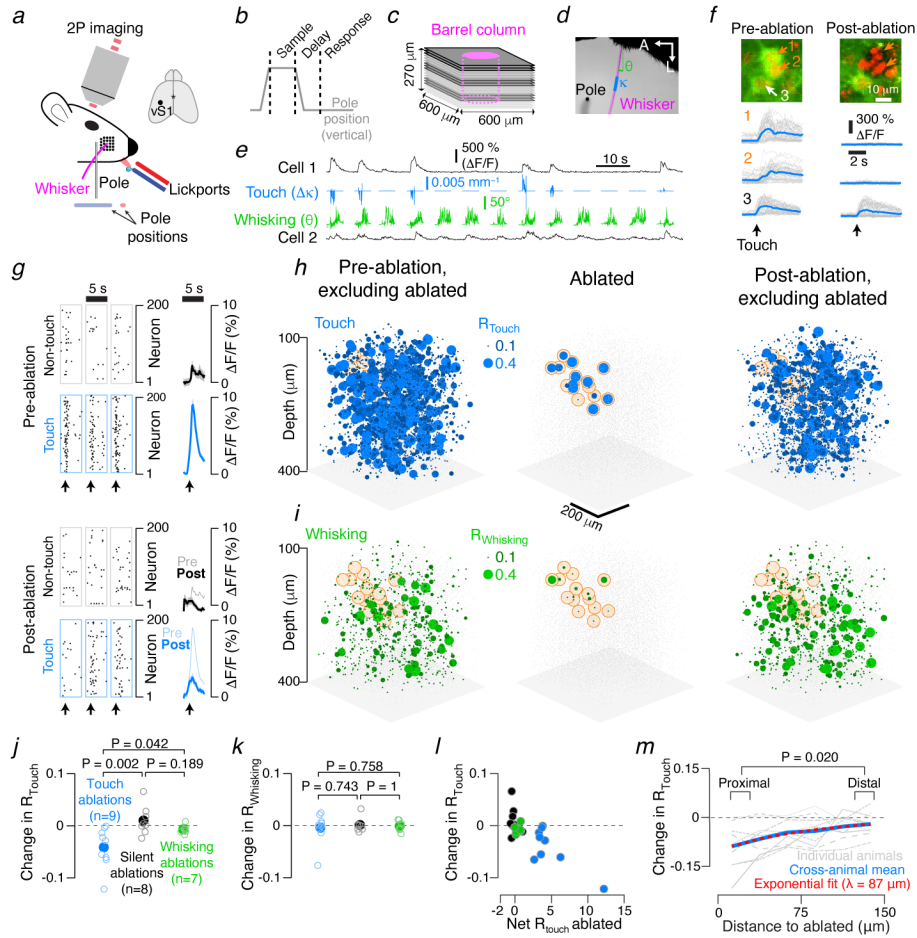


Figure 2. Barrel cortex touch networks are sensitive to ablation. **a.** Mice used one whisker to locate a pole and reported the perceived position by licking one of two lickports (red, blue). **b.** Task epochs (Methods). **c.** Imaging planes were centered on the barrel column of the spared whisker, magenta. Three planes were imaged simultaneously (same shade of grey). **d.** Example video frame showing the whisker (magenta), pole (black), whisker curvature (κ , blue), and whisker angle (θ , green). **e.** Neuronal activity for a touch (cell 1) and whisking (cell 2) cell. Blue, whisker curvature change (κ); green, whisker angle (θ). **f.** Ablations. Pyramidal neurons 1 and 2 (orange) were ablated (green, GCaMP6s; red, mCherry). Bottom, touch-aligned neuronal responses. **g-i.** Example experiment. **g.** Touch responses (dots, calcium events; Methods) for a subset of neurons before (top) and after (bottom) ablation. Grey boxes, 200 non-touch/non-whisking neurons; blue boxes, 200 touch neurons. Right, touch-aligned mean $\Delta F/F$ across these neurons for the strongest 5% of touches. Envelopes, s.e.m. **h.** Left, map for touch cells before ablation. Sphere size, R_{Touch} . Grey dots, other neurons. Orange, ablated neuron position. Center, R_{Touch} for ablated neurons. Right, R_{Touch} after ablation. **i.** As in **h**, but for whisking neurons. **j.** Effect of ablating different neurons on R_{Touch} in individual mice. Blue, touch ablations; black, silent neuron ablations; green, whisking ablations. P-values for Wilcoxon rank sum test between groups. **k.** As in **j**, but for R_{Whisking} . **l.** Ablation effect on change in R_{Touch} as a function of R_{Touch} summed over the

ablated neurons. Color as in **j. m.** Distance-dependence (w.r.t. closest ablated neuron) of post-ablation change in R_{touch} . Proximal change in P_{touch} : -0.132 ± 0.246 , grand median \pm adjusted MAD, distal: -0.056 ± 0.241 ; p-value for Wilcoxon signed rank test for proximal vs. distal medians, paired by animal, $N = 9$ mice.

Author Manuscript

Author Manuscript

Author Manuscript

Author Manuscript

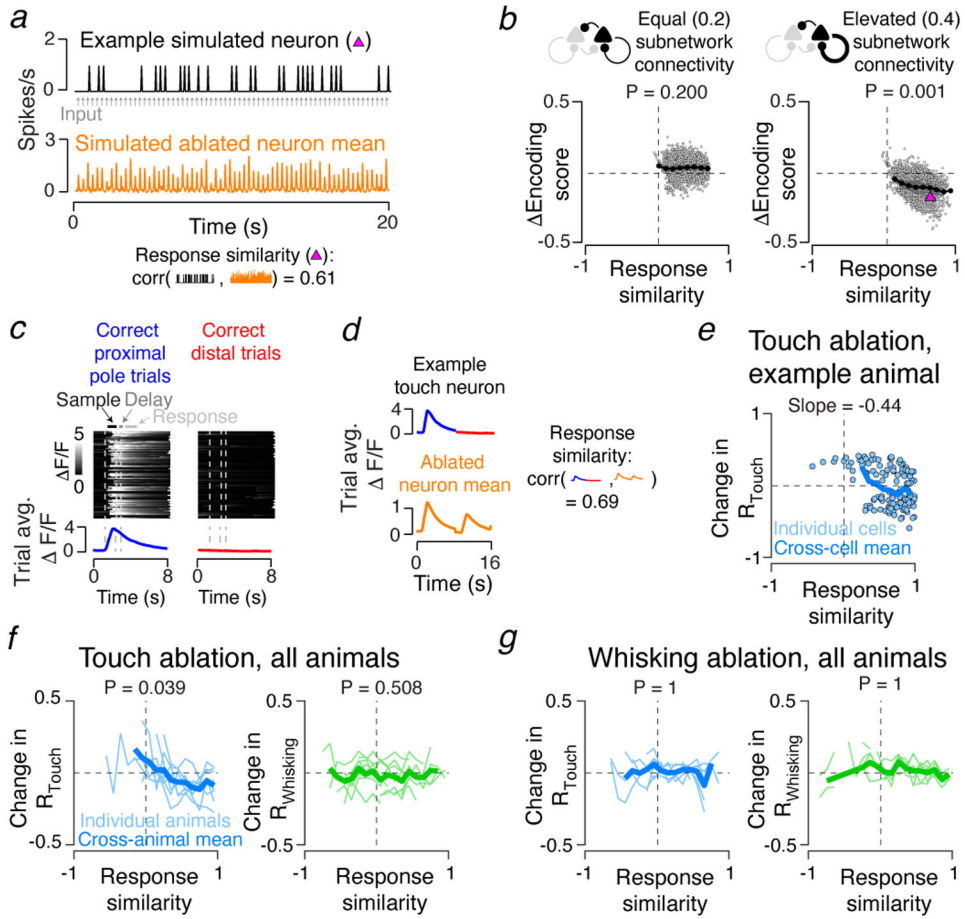


Figure 3. Effect of ablations depends on response similarity to ablated cells. **a.** Response similarity in simulated networks. Top, example neuron spike rate (black). Grey arrows, sensory input. Orange, mean spike rate across ablated neurons. Bottom, response similarity was computed by correlating neuronal spike rate with the mean ablated neuron spike rate. **b.** Dependence of post-ablation encoding score change on response similarity in model networks. Grey dots, individual neurons. Dark grey lines, single network averages; p-values for sign test that the slopes of linear fits across all networks ($N=30$; $P_{\text{conn}} = 0.2$ case: 3,779 neurons; $P_{\text{conn}} = 0.4$ case: 3,466 neurons) are 0. Black line, grand mean across networks. Magenta triangle, neuron from **a**. **c.** Trial averaged response for example touch neuron. Heat maps: $\Delta F/F$ for individual trials (proximal pole trials, left; distal, right). Bottom, trial averaged $\Delta F/F$. **d.** Top, trial averaged $\Delta F/F$ for neuron in **c**. Bottom, the mean trial averaged response across ablated neurons. Right, response similarity is the correlation of individual neuron trial averaged response vectors with the mean across ablated neurons. **e.** Touch neuron ablation induced changes in touch score as a function of response similarity in an example animal. Blue circles, individual neurons; blue line, binned mean (Methods). Slope for a linear fit of the points is given. **f.** Population data for all touch ablations for both touch (blue, left) and whisking (right, green) neurons. Thin colored lines, individual animal means for a given response similarity bin; thick lines, cross-animal mean. P-values for sign test that the slope of change in encoding score as a function of response similarity is 0 are given ($N=9$ mice;

2,768 touch neurons; 1,085 whisking neurons). **g.** As in **f**, but for whisking neuron ablation (N=7 mice; 1,692 touch neurons; 935 whisking neurons).

Author Manuscript

Author Manuscript

Author Manuscript

Author Manuscript